Journal of Bionic Engineering (2025) 22:1863–1880
https://doi.org/10.1007/s42235-025-00704-w

RESEARCH ARTICLE

A Novel Three-Dimensional-Printed Polycaprolactone/Nanohydroxyapatite-Nanoclay Scaffold for Bone Tissue Engineering Applications

Saba Nazari[1] · Seyed Ali Poursamar[2,3] · Mitra Naeimi[1] · Mohammad Rafienia[2] · Majid Monajjemi[1]

Received: 19 August 2024 / Revised: 24 March 2025 / Accepted: 27 March 2025 / Published online: 3 July 2025

Abstract
The field of bone tissue engineering has experienced an increase in prevalence due to the inherent challenge of the natural regeneration of significant bone deformities. This investigation focused on the preparation of Three-Dimensional (3D)-printed Polycaprolactone (PCL) scaffolds with varying proportions of Nanohydroxyapatite (NHA) and Nanoclay (NC), and their physiochemical and biological properties were assessed. The mechanical properties of PCL are satisfactory; however, its hydrophobic nature and long-term degradation hinder its use in scaffold fabrication. NHA and NC have been employed to improve the hydrophilic characteristics, mechanical strength, adhesive properties, biocompatibility, biodegradability, and osteoconductive behavior of PCL. The morphology results demonstrated 3D-printed structures with interconnected rectangular macropores and proper nanoparticle distribution. The sample containing 70 wt% NC showed the highest porosity (65.98 ± 2.54%), leading to an increased degradation rate. The compressive strength ranged from 10.65 ± 1.90 to 84.93 ± 9.93 MPa, which is directly proportional to the compressive strength of cancellous bone (2–12 MPa). The wettability, water uptake, and biodegradability of PCL scaffolds considerably improved as the amount of NC increased. The results of the cellular assays exhibited increased proliferation, viability, and adhesion of MG-63 cells due to the addition of NHA and NC to the scaffolds. Finally, according to the in vitro results, it can be concluded that 3D-printed samples with higher amounts of NC can be regarded as a suitable scaffold for expediting the regeneration process of bone defects.

Keywords Polycaprolactone · Hydroxyapatite · Nanoclay · 3D printing · Bone tissue engineering

1 Introduction

Bone defects can arise from various conditions, and while the skeleton possesses inherent regenerative capabilities, critical-sized defects necessitate intervention to promote accelerated bone regeneration. Tissue engineering bridges the gap between life sciences and engineering, offering alternative therapies aimed at improving organ function [1]. This interdisciplinary field focuses either on mimicking the natural tissue structure or providing scaffolds to support tissue regrowth. Bone-related diseases and traumas pose a significant global burden, leading to substantial advances in bone tissue engineering in recent years [2]. The key components in tissue engineering—cell sources, scaffolds, and growth signals—collaborate for effective tissue regeneration [3]. The bone scaffolds are expected to have proper porosity, biocompatibility, osteoconductivity, osteoinductivity, angiogenesis, degradability, and mechanical properties akin to bone [4]. Composite materials are increasingly used for scaffolds, combining the benefits of various materials [5]. These scaffolds improve chemical characteristics, degradation control, bioactivity, osteoconductivity and mechanical properties for bone regeneration [4]. Polycaprolactone

✉ Mitra Naeimi
mit.naeimi@iauctb.ac.ir

✉ Mohammad Rafienia
m_rafienia@med.mui.ac.ir

[1] Department of Biomedical Engineering, Central Tehran Branch, Islamic Azad University, Tehran, Iran

[2] Biosensor Research Center, Isfahan University of Medical Sciences, Isfahan, Iran

[3] Department of Biomaterials, Tissue Engineering and Nanotechnology, School of Advanced Medical Technologies, Isfahan University of Medical Sciences, Isfahan, Iran

(PCL), a semi-crystalline aliphatic polyester, is one of the synthetic polymers used in bone tissue engineering. Its high toughness and strength, low melting point, inherent tissue biocompatibility, easy dissolvability in most organic solvents, and low cost are the primary factors behind its popularity [2, 6]. However, PCL's hydrophobic nature and slow degradation can hinder bone regeneration [7]. To address these challenges, researchers have explored strategies such as the incorporation of a secondary ceramic phase into PCL scaffolds [8]. An example of such a phase is hydroxyapatite ($Ca_{10}(PO_4)_6(OH)_2$, HA), a key component of natural bone, which increases local Ca^{2+} concentration, thereby stimulating osteoblast proliferation and promoting mesenchymal stem cell differentiation [9]. Nanohydroxyapatite (NHA)'s extensive application in bone repair is attributed to its immunogenicity, biocompatibility, bioactivity, and effective bone conductivity [5]. Nevertheless, its intrinsic brittleness and insufficient mechanical strength limit its standalone use, necessitating the integration of NHA with other polymers to improve performance [10]. Nanoclays (NCs) are also a promising approach to incorporate into polymer matrix, particularly organically modified NCs like Montmorillonite (MMT). MMT minerals, serving as a significant bioactive NC, consist of platelets made of layered silicates possessing a distinct sandwiched structure. MMT minerals, which have a high specific surface area and aspect ratio, are a significant bioactive NC with excellent mechanical strength, chemical functionality, biocompatibility, degradability, and osteogenesis induction. The incorporation of NC minerals into nanocomposites has been shown to support in vitro biomineralization and osteogenic differentiation of mesenchymal stem cells, crucial for bone formation [11].

3D printing is an emerging method for creating medical alternatives and has great potential in tissue engineering [12]. With 3D printing, scaffolds with precise dimensions and complex shapes can be fabricated, offering adaptable and defect-filling structures for tissue regeneration. In bone tissue engineering, scaffolds must meet specific criteria, including appropriate geometry, porosity, biocompatibility, mechanical strength, and osteoconductivity [13].

Table 1 3D printing ink composed of varying proportions of components

Samples	Materials' weight ratio	PCL (w/w)	NHA (w/w)	NC (w/w)
PHN1	PCL/NHA (100 wt%)/NC (0 wt%)	60%	40%	–
PHN2	PCL/NHA (70 wt%)/NC (30 wt%)	60%	28%	12%
PHN3	PCL/NHA (50 wt%)/NC (50 wt%)	60%	20%	20%
PHN4	PCL/NHA (30 wt%)/NC (70 wt%)	60%	12%	28%
PHN5	PCL/NHA (0 wt%)/NC (100 wt%)	60%	–	40%

Recent research has focused on composites that combine the strengths of both synthetic and natural materials. In this context, an innovative nanocomposite scaffold was developed using PCL, NHA, and NCs, fabricated through 3D printing. The resulting PCL/NHA-NC composite scaffolds were evaluated for their morphology, chemical properties, mechanical strength, hydrophilicity, biomineralization, and degradability. Additionally, in vitro studies assessed the proliferation and adhesion of MG-63 cells, further confirming the scaffold's potential for bone regeneration.

2 Materials and Methods

2.1 Materials

Medium-sized 3 mm pellets of PCL (M_w = 60 kDa) and chloroform (99.8%) as PCL solvent were provided from Sigma-Aldrich (St. Louis, MO, USA) and Merck (Germany), respectively. The NHA used in this study (< 100 nm, plate-like morphology) was sourced from Pardis Pajouhesh Fanavaran Yazd Co. (Yazd, Iran), and NC (< 100 nm, sheet-like structure) was obtained from US Research Nanomaterials Inc. (Houston, TX, USA). The selection of plate-like NHA was based on our previous findings, which showed that this morphology enhances printability by reducing ink viscosity, even at higher concentrations, and increases bioactivity due to its less crystalline order [8]. All used cell culture media in this study were purchased from Thermo Fisher Scientific (Mumbai, India). Simulated body fluid (SBF), 4-(6,6-diamidino-2-phenylindole dihydrochloride (DAPI solution), 3-(4,5-dimethylthiazol-2-yl)-2,5-diphenyltetrazolium bromide (MTT), and Dimethyl sulfoxide (DMSO) were provided by Sigma-Aldrich (St. Louis, MO, USA).

2.2 Ink Preparation

A 50% (w/v) printable ink was prepared through dissolving PCL pellets in chloroform for 1 h at 40 °C. Subsequently, the PCL solution was combined with NHA and NC additives at the prescribed amount specified in Table 1. The finalized ink was continuously stirred in an open environment so that the solvent evaporated, adjusting the viscosity to an empirically determined viscosity suitable for 3D printing [14].

2.3 Scaffold 3D Printing

The prepared inks were printed using a 3D printer with a single-screw microextruder and a three-axis Extrusion-Based Printing (EBP) platform (Abtin II; Abtin Teb Iran Company). The scaffold geometry was designed using SolidWorks software (Solidworks version 2017; Dassault

Syste'mes, France), and the STL file was translated to G-code with Slic3r software. The G-codes were transferred to a 3D printer host, enabling output for 3D printing. Repetier Host (V2.1.6) 3D software was used for visualizing and modifying the G-code, with manual adjustments made to define additional parameters. The 20-layer porous structures were printed layer by layer via continuous ink extrusion with a 22G nozzle (410 µm inner diameter) after the ink was loaded into a 10 mL syringe. Scaffolds measuring $20 \times 20 \times 6$ mm^3, with an extrusion multiplier of 0.0096, speed of 4 mm/s, and 500 µm strut spacing, were manufactured at ambient temperature. Post-printing, the scaffolds were placed in a vacuum oven at 37 °C and 5 mbar for 4 h to eliminate residual solvent. The overall process of scaffold preparation can be observed in Fig. 1a.

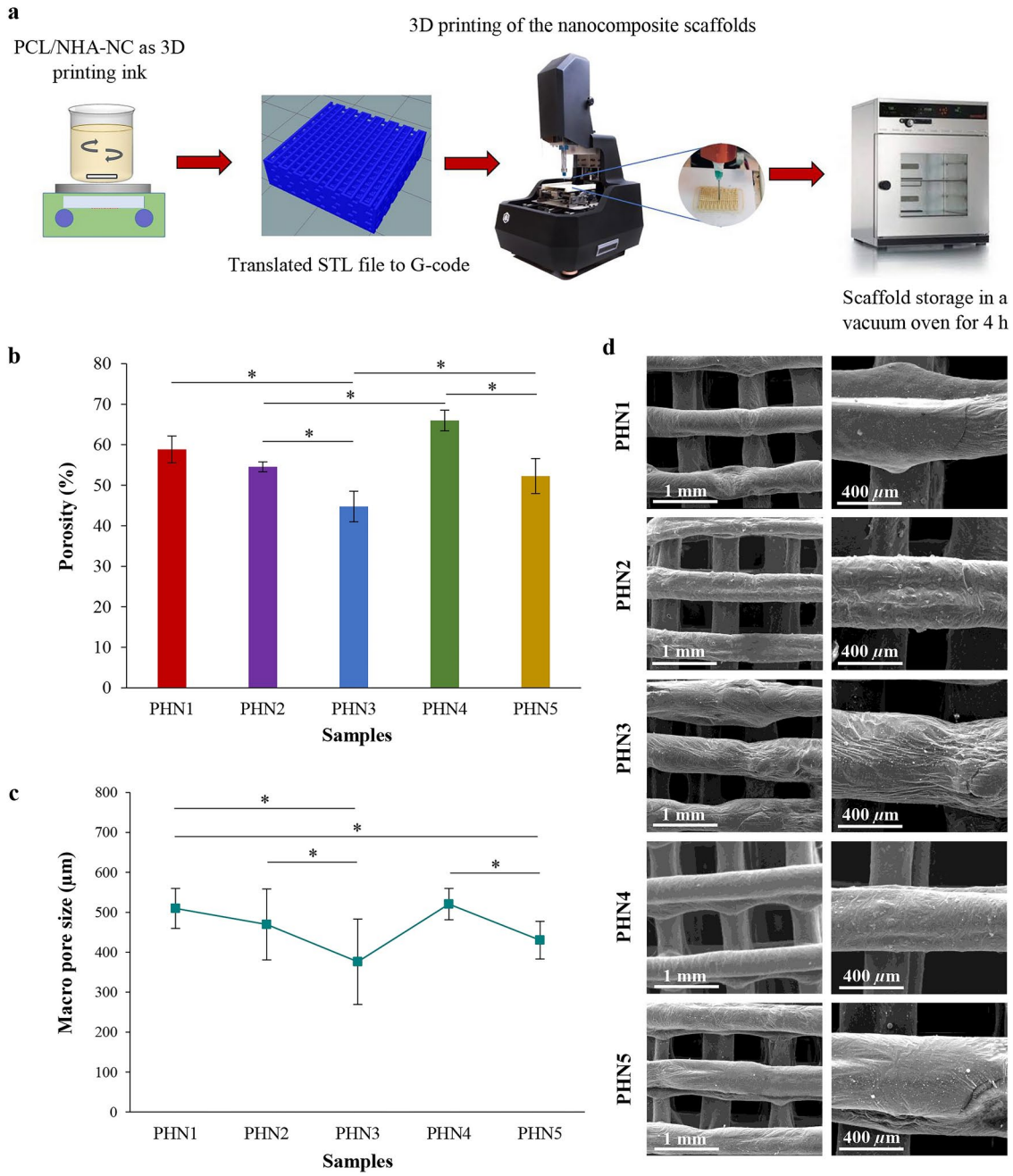

Fig. 1 **a** Preparation steps of the 3D-printed nanocomposite scaffolds. The 3D-printed scaffolds' **b** porosity percentage, **c** average pore size and **d** SEM images of the 3D-printed scaffolds at various scale bars (1 mm and 400 µm) with different amounts of NHA and NC (Values are mean ± *SD*, $n = 3$, $^*P \leq 0.05$)

2.4 The Scaffolds' Characterization

2.4.1 Porosity Measurement

The liquid displacement method was used to determine the porosity of the 3D-printed scaffolds. Hexane was selected as the transport fluid because it can penetrate through the scaffolds without changing the structure's dimensions [27]. A previously weighed scaffold was submerged for 5 min in a specific volume of hexane (V_1). Then, the hexane and hexane-impregnated scaffold's total volume (V_2) was measured. Following the removal of the scaffold, the volume of the remaining hexane was recorded (V_3). After three replications for each type of sample, the scaffold porosity was calculated using Eq. (1) as follows:

$$\mathrm{P} = \frac{\mathrm{V1} - \mathrm{V3}}{\mathrm{V2} - \mathrm{V3}} \times 100 \tag{1}$$

2.4.2 Morphological Observation

In order to evaluate the morphology of the scaffolds, the samples with a diameter of 5 mm were gold-plated, and 20 kV of accelerating voltage was used to take the Scanning Electron Microscopy (SEM) images (Philips XL30, Netherlands). Using Image J software (v.1.52a, National Institutes of Health, USA), macropores selected at random were additionally assessed for their diameter through SEM images of the scaffolds (taken at 50× magnification).

2.4.3 Scaffold Spectral Characterization

An FT/IR-6300 spectrometer (JASCO, Japan) was used to analyze the chemical composition of pure PCL, NHA, and NC as well as their nanocomposite scaffolds. It has a wave number range of 650 to 4000 cm^{-1} and a resolution of 4 cm^{-1}. Additionally, the examination of the phase shifts and purity of the scaffold materials was conducted by analyzing the recorded XRD patterns within an angular range of $15° \leq 2\theta \leq 80$, using X-ray diffraction (XRD; Bruker, D8ADVANCE/Germany). This analysis was performed using Cu Kα radiation ($\lambda = 1.540598$ Å). The analysis involved a step size of 0.05 degrees, with each step lasting for 2 s, and an applied voltage of 40 kV.

2.4.4 Mechanical Behavior

The compression strength and stiffness of dry scaffolds ($4.5 \times 4 \times 5$ mm^3) were measured using a universal testing machine (Hounsfield-H25KS-England) with a 2.5 KN load cell. After applying an axial load to the sample up to its 50% strain level at a loading rate of 5 mm/min, the compressive modulus was calculated using the slope of the elastic region (0–0.15 strain) of the obtained stress–strain curve. The compressive strength and strain values were also determined through the subsequent Eqs. (2 and 3):

$$\sigma = \frac{\mathrm{F}}{\mathrm{A}} \tag{2}$$

$$\varepsilon = \frac{\Delta L}{L_0} \tag{3}$$

where σ represents the compressive strength, F is the maximum compressive load applied, and A is the cross-sectional area of the scaffold. The compressive strain (ε) is derived from ΔL, the change in scaffold length under compression, and L_0, the original scaffold length before compression.

2.4.5 Contact Angle Measurement

The wettability of scaffolds is a critical chemical property, providing insights into their surface structure and composition. Static contact angles were measured using the sessile drop method with a CA-ES10 (Fars EOR. TechCo.) device at ambient temperature. A 5 µL water droplet was placed on the scaffold surface, and the contact angle was recorded 10 s later under controlled humidity ($n = 3$).

2.4.6 Water Uptake

Water uptake investigations were carried out utilizing dry-weighted scaffolds (W_d) with a dimension of 10×10 mm^2 submerged in PBS at 37 °C. At different time points of 1, 6, 12, 24, and 48 h [15], swollen samples were removed from the solution, and after absorbing the excess moisture with filter paper, their weight (W_w) was recorded [16]. The water uptake was calculated using Eq. (4) as follows:

$$\text{Water uptake}(\%) = \frac{\mathrm{W_w} - \mathrm{W_d}}{\mathrm{W_d}} \times 100 \tag{4}$$

2.4.7 Bioactivity and Ion Release

The Kokubo protocol [17] was used to test the bioactivity of 3D-printed scaffolds ($n = 3$ with 10 mm diameter) by submerging them in SBF at 37 °C for 7 and 28 days. Throughout the incubation period, the SBF solution was replaced twice a week, and the scaffolds were gently rinsed with pure water after each time point and dried in an oven at 60 °C for 4 h. The elemental distribution of calcium, phosphorus, and silicate was evaluated using EDX analysis in addition to the SEM examination of the lyophilized scaffolds. Moreover, induced coupled plasma spectroscopy was used to measure

the amounts of calcium and phosphorus ions released by the scaffolds (ICP, Pekin Elmer-Optima 7300 DV).

2.4.8 Evaluation of Degradation Rate

In order to investigate the 3D-printed scaffolds' degradation behavior, the scaffolds with cut dimensions of 5×5 mm^2 were submerged in PBS (pH 7.4) and maintained at 37 °C for 3 months in order to study the scaffolds' hydrolytic degradation behavior [18]. At specific time intervals, the scaffolds with previously identified weight (W_0) were first taken out of the solution, completely rinsed with distilled water, dried at 45 °C for 24 h in a vacuum oven, and weighed another time (W_t). The following Eq. (5) was used to obtain the degradation rate:

$$\text{Degradation rate}(\%) = \frac{W_0 - W_t}{W_0} \times 100 \quad (5)$$

During the degradation process, the pH changes were also assessed by employing a pH meter (ISTEK, P/Korea 240L) at weekly intervals for a duration of 3 months. Subsequently, the scaffolds were subjected to further investigation through the employment of FTIR, SEM, and EDX after the degradation rate was calculated at the final time point.

2.5 Cell Behavior on 3D-Printed Scaffolds

2.5.1 Cell Culture

In order to evaluate the bone cell behavior on the engineered scaffolds, the MG-63 cells were obtained from the Pasteur Institute, Tehran, Iran. The MG-63 cells are commonly employed as a model for osteoblasts in order to examine the viability, attachment, and proliferation of bone cells on scaffolds possessing load-bearing characteristics [19]. The cells were cultured in DMEM supplemented with 10% FBS, and 1% penicillin/streptomycin before being incubated at 37 °C and 5% CO_2 until the level of 80% confluency was reached. The scaffolds were disinfected using UV irradiation for 20 min. After cell trypsinization, the scaffolds in a 24-well plate were then seeded with a cell suspension (1×10^4 cells/well), and they were then moved to an incubator (37 °C, 5% CO_2).

2.5.2 MTT Assay

The MTT assay was implemented to evaluate the in vitro vitality of cultured MG-63 cells on each scaffold at 1, 3, and 7 days, in accordance with the ISO-10993–5 standard. At each time point, the culture medium was removed, and after washing the cell-seeded scaffolds with PBS, it was replaced with a medium containing MTT (0.5 mg/mL). Then, the MTT solution was removed after 4 h of incubation, and 200 µL of DMSO was then added to each sample ($n=3$). The obtained solution was put into a 96-well microplate, and an ELISA reader (Bio-tek FLx800, USA) was used to find the Optical Density (*OD*) at a wavelength of 570 nm. A monolayer culture of cells was considered the control group. The cell viability (%) was normalized by the control group (monolayer culture of cells) using the following formula (6):

$$\text{Cell viability } (\%) = \frac{\text{Sample wells OD} - \text{Blank OD}}{\text{Control wells OD} - \text{Blank OD}} \times 100 \quad (6)$$

2.5.3 SEM Imaging

To evaluate MG-63 cell adherence and morphology, SEM images of cell-seeded scaffolds were obtained using a Philips XL30 microscope (Netherlands). Cells were seeded on scaffolds for one day before the culture medium was removed and treated with 3% glutaraldehyde for 2 h in a refrigerated environment. The samples were then dehydrated through an ethanol sequence of 50, 70, 90, and 100% for 10 min each. After gold-coating the samples, they were prepared for SEM imaging.

2.5.4 DAPI Staining

After 7-day incubation of cell-cultured scaffolds, the culture medium was removed, the samples were rinsed with PBS, and they were subjected to 4% paraformaldehyde for 20 min before being submerged in a solution containing 1 µg/mL DAPI for 10 min. Finally, a fluorescent image analyzer (Nikon Eclipse Ti, Japan) was used to take images of cultured MG-63 cell nuclei.

2.6 Statistical Analysis

Every measurement was repeated at least three times. The acquired outcomes of this study were displayed in the form of a mean ± Standard Deviation (*SD*). One-Way Analysis of Variance (ANOVA) and Tukey's HSD post-hoc test for independent samples were used to identify significant differences between the groups (SPSS software V.23). Statistical significance was defined as a value of $P \leq 0.05$.

3 Results and Discussion

3.1 The Porosity, Morphology, and Macropore Size of the Scaffolds

Biodegradable polymer-based porous scaffolds are essential in tissue engineering for regulating cellular functionality and developing new tissues and organs. The macropore architecture of these scaffolds must facilitate effective cell seeding, penetration, and dispersion [20]. The porosity of 3D-printed samples, shown in Fig. 1b, revealed that decreasing NHA and adding NC in a 50/50 ratio reduced porosity from 58.84 ± 3.30 to 44.75 ± 3.76%. The PHN5 sample showed a relatively low porosity of 52.26 ± 4.31%, while increasing NC concentration to 70 wt% resulted in the highest porosity of 65.98 ± 2.08% ($P > 0.05$). In 3D printing, the structure of macro and micro pores is influenced by the formulation of the printing ink [14]. The current investigation demonstrates that the combination of NC and NHA in a 30/70 ratio enhances the ink composition for fabricating 3D samples. This enhancement is evident from the examination of ink viscosity and SEM images, revealing improved printability and uniform filament formation. Moreover, the decrease in PHN3 porosity is linked to the ink formulation, as the ink obtained by combining equal amounts of NHA and NC results in a printing ink with reduced viscosity and ultimately smaller porosity holes.

Figure 1c and d illustrate the morphology and average macropore diameters of the composite scaffolds. SEM images revealed an interconnected, rectangular macropore structure in all 3D-printed samples, with distinct distribution of NHA and NC particles on the scaffold surface. The filament structure was consistently precise across all scaffolds, with no observable cracks, micropores, or shrinkage on the strands, ensuring structural stability under mechanical loading [21].

Incorporating 70 wt% NC with 30 wt% NHA reduced filament diameter, resulting in the largest average macropore size in the PHN4 sample at 520.51 ± 39.21 µm. This was statistically significant compared to samples with lower NC proportions ($P \leq 0.05$). NCs, as inorganic fillers, can enhance porosity due to their electrostatic interactions and distribution within the polymeric ink [22]. Previous research has demonstrated that an elevation in MMT quantity results in a rise in scaffold surface tension [23], which reduces filament diameter and enlarges macropore size [24]. Furthermore, increased surface tension has been demonstrated to improve printability and resolution by reducing defects caused by satellite droplets. This enhanced stability of the filament and reduced ink spreading ultimately lead to a higher porosity percentage within the printed samples [8, 22]. Research has also demonstrated that NCs exhibit thixotropy, where ink thickens under pressure but recovers upon release, crucial for maintaining structural precision during and after printing. Additionally, sheet-like NCs function as a rheological modifier by exhibiting inherent shear-thinning behavior due to their opposing surface charges, which prompt structural recovery at rest and breakdown under applied shear. This feature allows the ink to uphold its structure at rest while thinning under pressure during printing, ultimately enhancing overall viscosity. The elevated viscosity is advantageous for extrusion-based 3D printing as it promotes stable filament formation, while the shear-thinning property facilitates smooth extrusion through the printer nozzle [25–27]. Consequently, the increased macropore size noted in this investigation can be attributed to alterations in particle dispersion, NC inner structure, and increased surface tension, primarily associated with a higher concentration of NC rather than NHA. The PHN3 sample exhibited a notable decrease in porosity diameter, and the obtained image provided additional supporting evidence of the low viscosity of the ink as well as a resulting increase in the diameter of the filament. This observation suggests that the printability of this particular sample presents a considerable challenge. Prior research has demonstrated that optimal bone growth in scaffolds requires porosity and macropore sizes of at least 50% and 300–800 µm, respectively, to support angiogenesis and cell migration [8, 28]. As a consequence, the prepared scaffolds demonstrate structural capacity for bone tissue engineering, with NHA and higher NC proportions enhancing overall porosity in PCL/NHA-NC scaffolds.

3.2 Spectroscopic Evaluations of the Nanocomposite Scaffolds

The pure PCL, NHA, and NC functional groups as well as their composites were assessed using FTIR, and the findings are shown in Fig. 2a. The FTIR spectra of PCL revealed that the strong peak at 1721 cm^{-1} corresponded to C=O stretching, whereas the peaks at 2865 and 2941 cm^{-1} belonged to symmetric and asymmetric CH_2 group stretching, respectively. The C–O–C group appears to have undergone symmetric stretching in the band at 1159 cm^{-1}, whereas asymmetric C–O–C stretching occurred between 1240 and 1294 cm^{-1} [2]. The primary peaks in the NHA spectrum are located at 3421, 1630, 1036, 976 cm^{-1} which are attributed to the vibrations of OH stretching vibrations, OH group bending, carbonate group vibration, asymmetric stretching of PO_4^{3-}, and symmetric stretching of PO_4^{3-}, respectively [29]. The characteristic peaks of NC's FTIR spectrum can be detected at 797 cm^{-1} (Si–O–Al vibration), 1033 cm^{-1} (Si–O–Si stretching), 1637 and 3425 cm^{-1} (O–H stretching of absorbed H_2O in NC), and 3623 cm^{-1} (stretching mode of the Si–OH and Al–OH in the silicate layers of NC) [30]. The

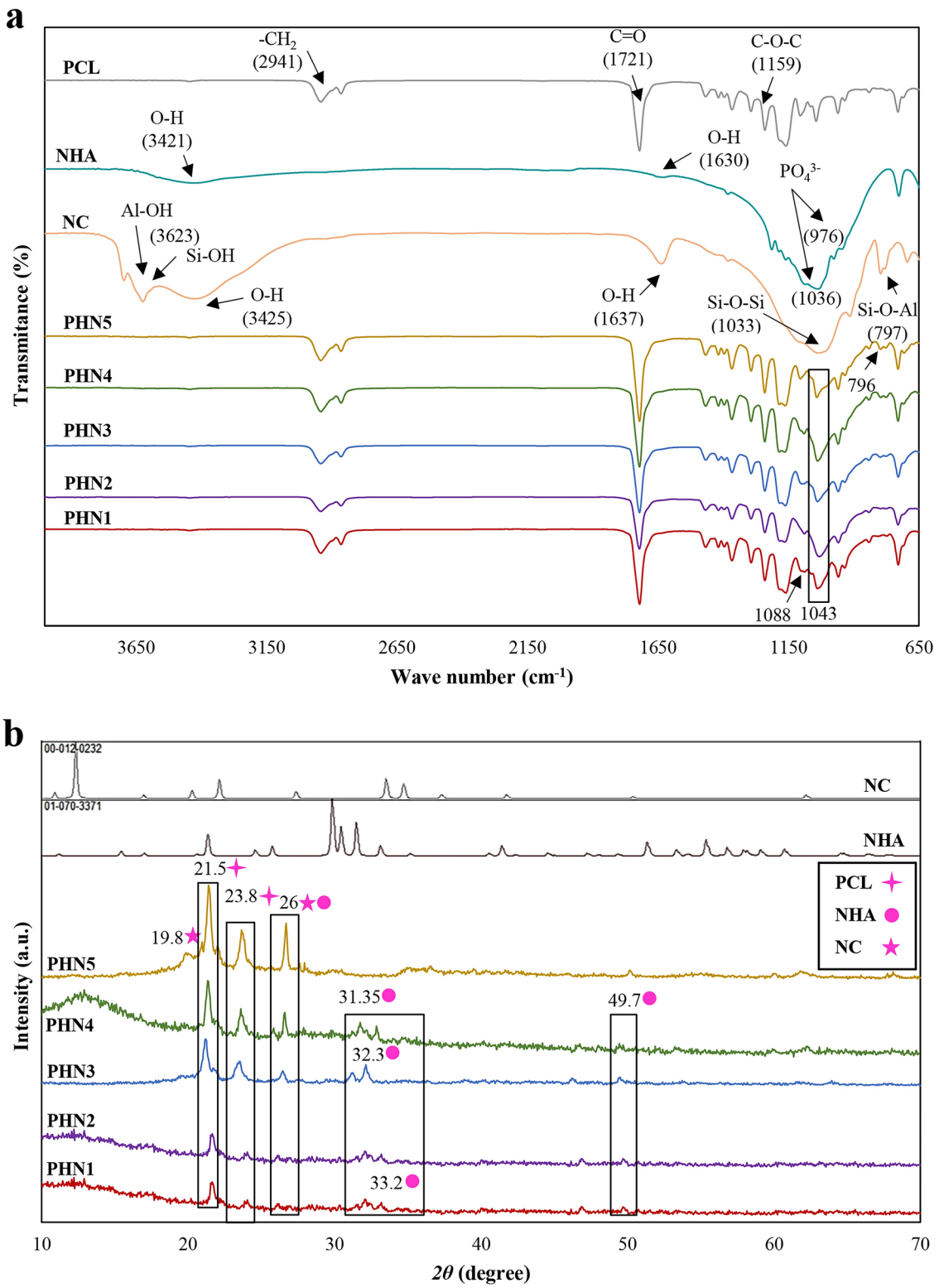

Fig. 2 **a** FTIR spectra of pure PCL, NHA and NC and PCL/NHA-NC scaffolds (100:0, 70:30, 50:50, 30:70, and 0:100), and **b** the scaffolds' XRD patterns

composite scaffolds exhibited generally similar spectra, with distinct PCL peaks observed in all the spectra due to their higher incorporation. It is evident that when the concentration of NC rises, the 796 cm^{-1} peak gets stronger. Additionally, a peak at 1088 cm^{-1} was seen in the sample with the highest concentration of NHA, indicating its presence in the scaffold. The PCL's sharp peak at 1043 cm^{-1} transformed into a broad peak with the increase in NHA concentration, thus indicating an overlap of this peak with the peak at 1036 cm^{-1} attributed to NHA. In general, the FTIR pattern of the composite scaffolds made it clear that the distinctive bands of PCL, NHA, and NC can be identified.

The XRD patterns of the samples are presented in Fig. 2b. It was observed that the 3D-printed scaffolds revealed two typical peaks at 2θ=21.5° and 23.8°, indicating the crystal structure of PCL [31, 32]. The existence of peaks at around 2θ=26.2°, 31.35°, 32.3°, 33.2°, and 49.7° in the XRD pattern suggested the crystal-like characteristics of NHA powder that was integrated into the structures [33]. These peaks were found to correspond with JCPDS Card No. 01-070-3371. Furthermore, XRD analysis of the scaffolds containing NC revealed the introduction of polymer chains into the NC interlayer domain. This was confirmed by the presence of characteristic peaks of NC at 2θ=19.8° and 26°, as indicated by JCPDS Card No. 00-012-0232 [34, 35]. These results suggest that there may be interactions between molecules in the PCL/NHA-NC scaffold.

3.3 Mechanical Characterization

The bioink used in bone tissue engineering must possess mechanical properties suitable for load-bearing, stiffness and structural integrity of 3D-printed scaffolds [36]. This investigation examined the compressive strength and stiffness of the prepared scaffolds. Stress–strain curves at 50% strain (Fig. 3a) showed variations in PHN3 but consistent elastomeric behavior across all samples, aligning with PCL-based porous scaffolds [37, 38]. The data presented in Table 2 and Fig. 3b and c indicate that the PHN1 sample, compared to other scaffolds, exhibited the lowest compressive modulus, which can be attributed to the properties of NHA. The intrinsic brittleness of NHA in combination with the flexible PCL polymer may intensify the brittleness of PCL/NHA samples and result in a reduction of their compressive strength and stiffness. In fact, the use of composite scaffolds that contain NHA may result in the accumulation of crystals. These enlarged NHA crystals have the potential to act as cracks within the scaffold. This is due to the limited bonding between the crystals and the polymer matrix, as well as their restricted impact on the reinforcement mechanism [49, 50]. On the other hand, the PHN3 sample exhibited the highest compressive strength (82.93 ± 9.93 MPa) and modulus (117.19 ± 6.62 MPa), which can be attributed to the reduced macropore size resulting from the experimentally observed low viscosity, as also evident in the SEM image ($P \leq 0.05$). This observation suggests that the equal proportion of NHA and NC plays a significant role in influencing intra-structural changes, which contribute to the enhanced mechanical properties. A previous study reported a zeta potential of -38.4 mV for plate-like NHA, indicating a strong negative surface charge and excellent colloidal stability. This stability arises from significant electrostatic repulsion between particles, which is crucial for maintaining uniform dispersion in the bio-ink and preventing particle aggregation [8]. In the current study, the 50:50 combination of NHA and NC likely results in similarly stable suspensions, as demonstrated by the experimentally observed low viscosity of the bioink. The negatively charged surface of NC may further enhance the zeta potential of the system, reducing the viscosity of the ink and leading to the formation of smaller macropores. Previous research has established an inverse relationship between porosity and mechanical properties, with an increase in porosity size typically leading to a decrease in mechanical strength [39, 40]. The results of this study confirm this trend, with the sample containing 100 wt% NC exhibiting the second-highest compressive strength (17.13 ± 4.03 MPa) following the PHN3 sample. However, this difference was not statistically significant ($P > 0.05$). In contrast, the PHN4 sample exhibited the highest modulus (40.23 ± 4.22 MPa), indicating superior resistance to deformation relative to the other samples ($P \leq 0.05$). Furthermore, the results demonstrate that the compressive properties of PCL/NHA scaffolds increased with the addition of NC, and for the PHN4 sample, the compressive strength was largely unaffected by the scaffold porosity. Specifically, despite the PHN4 sample having the highest porosity, its compressive strength not only remained unaffected but was also greater than that of samples with higher NHA proportions. These findings suggest that the incorporation of NC plays a critical role in enhancing the mechanical properties of the scaffolds, irrespective of porosity, and underscores the importance of the NHA-NC combination in optimizing both structural integrity and material performance. The use of NC nanosheets as an inorganic filler can enhance scaffold strength by promoting homogeneous distribution and interaction between the polymer matrix and nanosilicates [11]. The enhanced mechanical properties in polymer/NC composite systems can be attributed to the presence of nano-thick layers within the clay material, as well as the larger surface area and higher aspect ratio of clay particles [41]. The interlocking structure formed by the combination of polymer and MMT in composite materials restricts polymer chain movement, enhancing interaction between the two phases under external forces. This

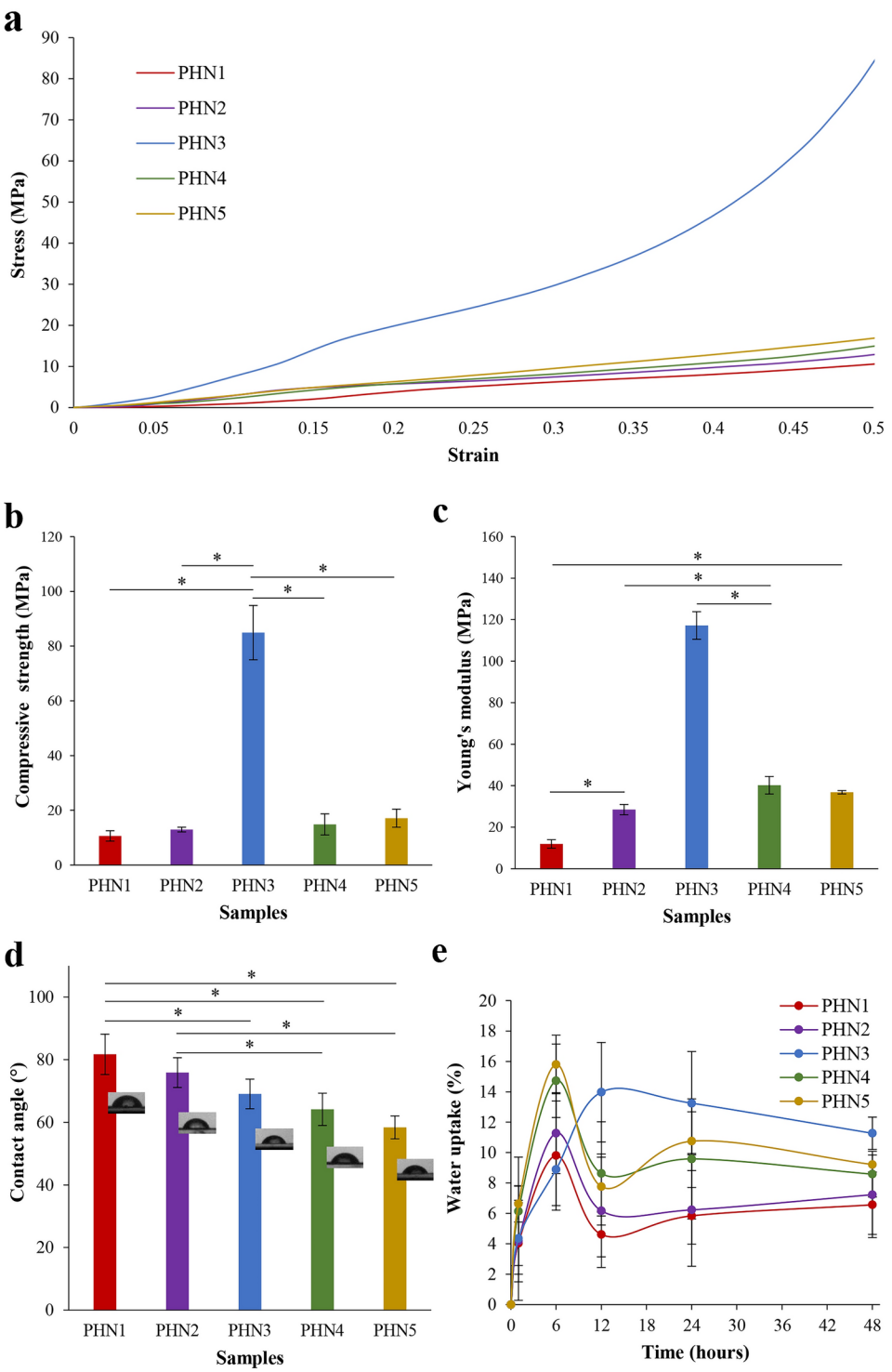

Fig. 3 **a** The stress–strain curves for the scaffolds under compression loading. The 3D-printed scaffolds' **b** compressive strength and **c** compressive moduli. The 3D-printed nanocomposite scaffolds' **d** water contact angle and **e** water uptake after 1, 6, 12, 24, and 48 h incubation in PBS (Values are mean ± *SD*, $n=3$, $^{*}P \leq 0.05$)

Table 2 The compressive strength, modulus and average contact angle of the 3D-printed samples

Samples	Compressive strength (MPa)	Compressive modulus (MPa)	Average contact angle (°)
PHN1	10.65 ± 1.90	11.95 ± 2.04	81.72 ± 6.44
PHN2	12.97 ± 0.86	28.47 ± 2.48	75.89 ± 4.79
PHN3	84.93 ± 9.93	117.19 ± 6.62	69.07 ± 4.72
PHN4	14.85 ± 3.85	40.23 ± 4.22	64.15 ± 5.14
PHN5	17.13 ± 3.29	36.83 ± 0.80	58.38 ± 3.63

interlocking increases molecular forces and contact area, leading to a greater number of interlocks, which improves the mechanical properties of polymer bone scaffolds [35]. When comparing the mechanical properties of human bone to those of 3D-printed scaffolds, it is evident that cortical bone remains significantly stronger (which has a strength range of 100–230 MPa and stiffness range of 7–30 GPa [42, 43]); while cancellous bone exhibits similar strength (with a range of 2–12 MPa) and stiffness (with a range of 0.01–3 GPa) [43, 44] to the composite scaffolds.

3.4 Wettability of the Scaffolds

Surface hydrophilicity is a key factor in predicting how materials interact with cells and biological media, influencing cell proliferation, attachment, and osteointegration in bone scaffolds [45]. Water contact angle tests (Fig. 3d; Table 2) revealed that the PHN1 sample had the highest contact angle (81.72 ± 6.44°), while the PHN5 sample had the lowest (58.38 ± 3.63°). Even though the PHN4 sample had no significant difference from the PCL/NC scaffold ($P > 0.05$), they both had a marked difference compared to the PCL/NHA sample ($P \leq 0.05$). A water droplet with a contact angle greater than 90° is indicative of a hydrophobic surface, which results in poor wetting and adhesion and low solid surface-free energy [46]. Prior research indicated that pure PCL has low hydrophilicity, with a contact angle over 100°, confirming its hydrophobic nature [47]. Nitya et al. found that the hydrophilicity of PCL augmented with an increase in the NC content [48]. Additionally, studies have found that the wettability of PCL scaffolds increases after the incorporation of NHA, due to the hydrophilic properties of NHA and the formation of extra crystallites on the surface of the scaffolds, resulting in an increase in surface roughness and contact angle. [49, 50]. However, this study demonstrated that the addition of NC had a more considerable influence on the hydrophilicity of PCL scaffolds than the incorporation of NHA.

3.5 Water Uptake of the Scaffolds

The water uptake capability of the scaffolds fabricated was observed at various time intervals, as shown in Fig. 3e. The inclusion of NC exceeding 50 wt% resulted in two primary and secondary peaks of water uptake after 6 and 24 h. In contrast, scaffolds with predominantly NHA showed a single peak at 6 h, with the PHN1 sample exhibiting the lowest water uptake (9.80 ± 5.58%). Furthermore, these samples commenced the process of water uptake subsequent to desorption, after a duration of 12 h. In general, the addition of NC led to a higher water uptake peak, with the PCL/NC scaffold recording 15.79 ± 6.95% after 6 h. The delayed water uptake peak observed at 12 h for the PHN3 scaffold (13.97 ± 3.26%) can be attributed to its distinct structural and morphological characteristics. The low viscosity of the ink allowed PHN3 to form thicker filaments and smaller macropores, which impede the rapid penetration and distribution of water within the scaffold [51]. This structural arrangement likely reduces the initial absorption rate, resulting in a longer period for the scaffold to reach its maximum water uptake capacity.

The ability of scaffolds to swell is vital as it regulates nutrient and metabolite exchange among cells [52]. PCL, being hydrophobic, resists water uptake, but combining it with NHA and NC has been shown to enhance water absorption. The introduction of NHA into PCL improves swelling due to the interface formed between NHA and the PCL matrix, allowing solvent penetration [53]. At a pH of 7.4 in PBS, the=O group in PCL becomes charged ions, contributing to the swelling behavior of the composite through increased electrostatic repulsion between these ionized groups [54]. This study found that NC had the most significant impact on enhancing water uptake, attributed to its hydrophilic nature, which facilitates the hydration of inorganic cations in the interlayer [52]. In general, the swelling effect of the MMT interlayer domain is well-established, especially in liquid or molten environments, where it expands, facilitating intercalation between polymer molecular chains. When exposed to a mixed solution with polymer, MMT absorbs water, leading to the expansion of the interlayer domain and enabling the polymer chains to embed within it, while the other end remains compatible with the polymer matrix. The combination of covalent or noncovalent intermolecular interactions and the mutual compatibility of organic materials is anticipated to produce intercalated molecular chains that serve as a connecting link between MMT and polymers. This process generates a molecular cross-linking bridge between inorganic and organic substances [35]. The use of both NHA and NC in PCL scaffolds appears to be a viable approach for regulating water release rate and augmenting water uptake.

3.6 Bioactivity and Ion Release Behavior

The evaluation of a biomaterial's capacity for osseointegration is commonly established through an examination of HA

growth on the surface of the scaffold. In accordance with Hench's theory, the commencement of NHA creation is initiated by the dissolution and liberation of calcium ions from the surface of the sample into the solution [55]. In this study, EDX analysis after 7 days of submersion in SBF revealed that higher NHA concentrations enhance calcium and phosphorus levels on the scaffold surface (Fig. 4a). The inclusion of calcium and phosphorus cations within the synthesized NHA present in the scaffold enhances the deposition of these elements. In instances of ion exchanges between the scaffold and the SBF solution, there exists a competitive relationship between Ca^{2+} and Mg^{2+} cations, in terms of their deposition and interaction. To promote crystalline NHA formation, the deposition of MgO and Mg_2SiO_4 must be minimized. Regarding the data acquired, it can be observed that there has been a reduction in the quantity of Mg present in the PHN1 sample. This reduction suggests that Ca^{2+} holds dominance over Mg^{2+} in terms of their interaction with the scaffold. Furthermore, there has been a decrease in the formation of MgO and Mg_2SiO_4 phases. Additionally, an increase in Mg in NHA-free scaffolds indicates that NHA compounds influence calcium-phosphate deposit formation. After 28 days, the PHN1 and PHN2 scaffolds demonstrated higher calcium and phosphorus levels compared to the other samples. Notably, the Ca/P ratios across all samples were consistent with that of biological apatite (1.67). PCL, a bioactive polymer, undergoes hydrolysis under physiological conditions, forming carboxylic (-COOH) groups on its surface and releasing H^+ ions into the SBF solution. The liberation of H^+ results in a concomitant escalation in the proclivity to dissolve the scaffold surface. In addition, it yields COO^- ions at the surface of the scaffold, thereby instigating electrostatic attraction between the PCL and Ca^{2+} ions that are present in the SBF [56]. In general, the generation of calcium-phosphate deposits is facilitated through the electrostatic attraction and repulsion that take place between the positive and negative ions of the SBF medium and the scaffold surface [55]. The bioactivity of composite scaffolds, based on PCL and NHA, is linked to PCL degradation and NHA nanoparticle dissolution. Under physiological pH, PCL's acidic degradation releases COO^- ions, while negatively charged NHA particles help absorb Ca^{2+} ions, promoting calcium-phosphate mineralization [57]. Higher NHA content in scaffolds increases nucleation sites, leading to greater apatite formation. Additionally, NC possesses a negatively charged surface, which exhibits a synergetic effect with NHA in inducing apatite formation [58]. The inclusion of SiO_4^{4-} from NC is notable in the generation of negatively charged silanol (Si–OH) layers that may induce the electrostatic adsorption of Mg^{2+} and Ca^{2+} onto the scaffold's surface [59]. Upon the formation of apatite nuclei, spontaneous growth may ensue through the utilization of calcium and phosphate ions that are readily available in the surrounding fluid.

Based on ICP findings in Fig. 4b and c, the SBF solution of the scaffold containing 100 wt% NHA exhibited higher calcium and phosphorus ion concentrations than other scaffolds, suggesting a higher NHA dissolution rate. This led to the liberation of calcium and phosphate ions, enhancing their solution concentration [56]. Notably, the surface roughness induced by the presence of NC constitutes an additional efficacious factor in the genesis of nucleation sites [59]. Data showed that the scaffold with 100 wt% NC had lower calcium and phosphorus levels compared to others over 28 days. On the other hand, scaffolds lacking NC exhibited decreased calcium and phosphorus levels in solution, suggesting enhanced interaction of these elements with the scaffold surface. Ion exchange, crucial for calcium-phosphate deposit formation, was inferred from the release of anions and cations into the solution upon immersion in SBF [55]. This process increased phosphorus levels through the release of HPO_4^{2-} and Mg^{2+} ions from the scaffold surface, while calcium concentrations rose due to deposition driven by the reduced phosphate ion levels and the subsequent incorporation of calcium cations onto the scaffold surface. Elemental analysis conducted on days 7 and 28 confirmed the superior nucleation and deposit formation of the 70:30 NHA/NC scaffold compared to the 30:70 NHA/NC scaffold ($P \leq 0.05$), emphasizing the critical role of NHA in mineral formation. In general, an augmentation in the quantity of calcium-phosphate deposits can be observed across all scaffolds during the 28-week period, which signifies the bioactivity of the scaffolds. PCL generates COOH groups that interact with the calcium and phosphate ions in SBF, thereby promoting the deposition of hydroxyapatite crystals on the scaffold surface [56]. The incorporation of COO^- in conjunction with the generation of Si–OH anionically charged cyanol layers actively engages in the attraction of Mg^{2+} and Ca^{2+} cations. The cationic attraction results in the formation of nucleation sites on the scaffolds' surface. The substrate's chemical and morphological provision, which is shown by the presence of cations and the roughness of the surface caused by the presence of NC, as well as the bioactivity of NHA and NC integrated into the scaffold's structure, are important factors in producing the bioactive properties. After introducing the positively charged substrate induced by calcium deposits, the anions HPO_4^{2-} and SiO_4^{4-}, originating from silicate layers present in NC, interact with the cations on the surface through the electrostatic attraction between opposite charges. The interaction observed between calcium cations and HPO_4^{2-} anions results in a reduction of the energy barrier for the generation of calcium-phosphate crystal deposits, thereby promoting their formation [60].

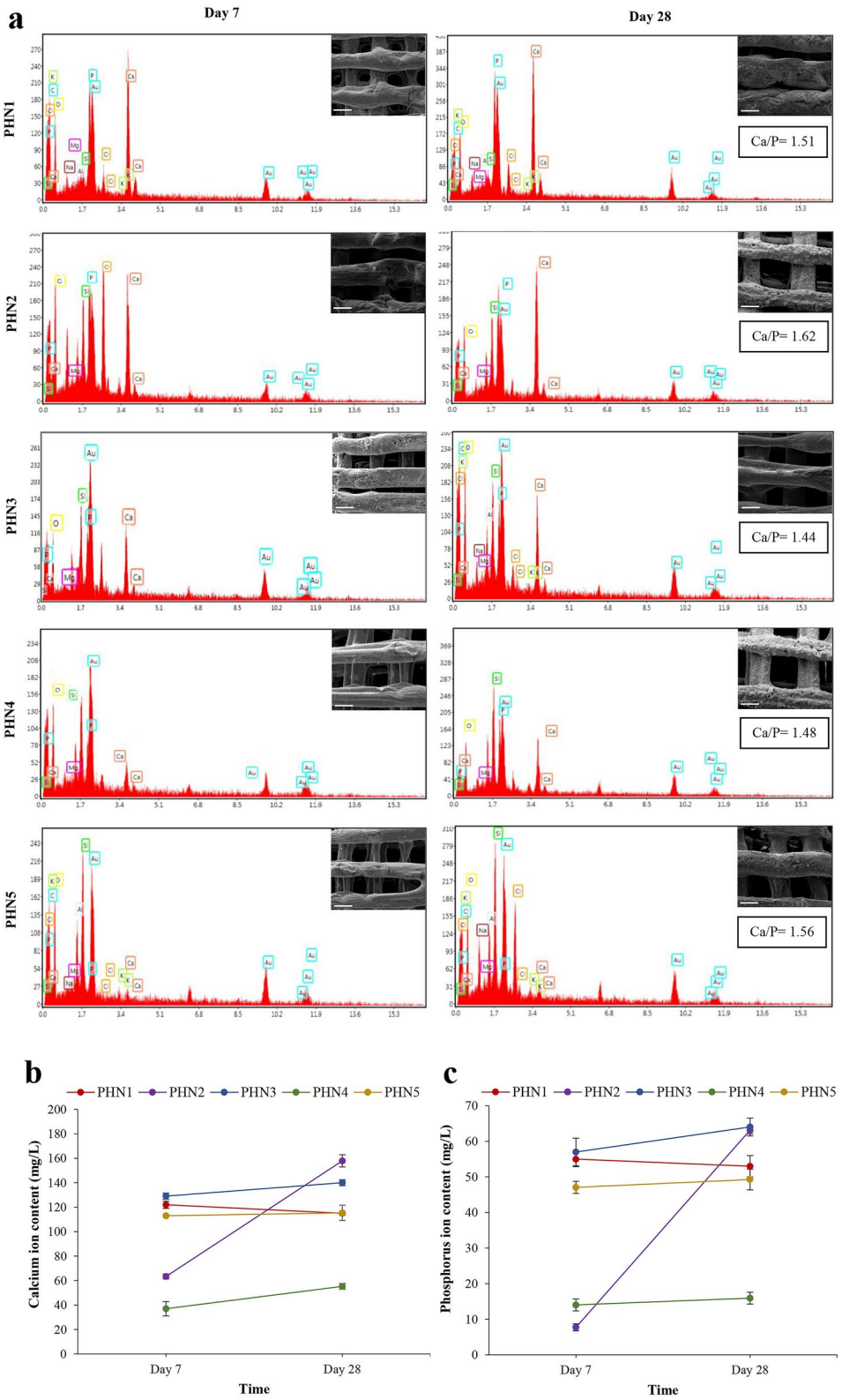

Fig. 4 **a** Elemental analysis of PHN1 to PHN5 samples with SEM images after 7 and 28 days of immersion in SBF to demonstrate the presence of calcium and phosphorus elements on the samples' surface (scale bars = 200 µm). **b** Calcium and **c** phosphorus ion contents (mg/L) of PHN1 to PHN5 samples in SBF during 1 and 4 weeks

3.7 Biodegradability

In bone tissue engineering, it's essential to modify scaffold degradation rates to provide structural support until the new bone reaches sufficient strength [61]. This study assessed the degradation of nanocomposite scaffolds over 12 weeks in PBS (pH 7.4). Results, shown in Fig. 5, include weight and pH changes, along with FTIR, EDX, and SEM images of the degraded samples after 12 weeks. All samples showed weight variations, including both increases and decreases, until the tenth week (Fig. 5a). Upon exposure to an aqueous or physiological environment, porous scaffolds engage with water molecules to initiate hydrolysis, a process involving absorption, interaction, and release [62]. These scaffolds also underwent cycles of water absorption and desorption, which resulted in fluctuating rates of weight loss. After 12 weeks, the highest and lowest degradation rates showed significant weight losses of 0.55±0.15 and 0.04±0.01%, respectively ($P \leq 0.05$). It could potentially be attributed to the considerable porosity of this scaffold, as well as the presence of NC. An increase in porosity percentage results in an augmentation of the surface area and contact with agents that induce degradation, such as enzymes or hydrolytic fluids. This ultimately leads to an accelerated degradation process due to the enhanced availability of sites for the occurrence of degradation reactions [63]. Additionally, negatively charged groups in NC, along with polar groups in PCL and HPO_4^{2-} and Ca cations from NHA, can augment the propensity of hydrolysis and chemical interactions. The ability of the prepared scaffolds to absorb water is influenced by various components, including PCL ester groups, silicate in NC, and phosphate and calcium ions in the NHA structure. On the contrary, hydrophilic scaffolds degrade at a faster rate in comparison to hydrophobic scaffolds due to the increased water uptake capacity exhibited by hydrophilic materials, which subsequently leads to enhanced swelling and subsequent degradation [64]. As previously stated, the incorporation of NC at concentrations of 70 and 100 wt% into the scaffolds resulted in an elevation of scaffold hydrophilicity, which was attributed to the presence of oxygen groups within the SiO_4^{-4} structure. This resulted in a substantial reduction in weight compared to other samples ($P \leq 0.05$).

All scaffolds displayed pH fluctuations over 12 weeks (Fig. 5b), likely due to ion exchanges and electrostatic interactions between charged groups [59, 65]. The ester groups in PCL react with the aqueous environment, generating water and acid, which leads to a decrease in pH. This decrease in pH has a positive effect on the solubility of NHA [55, 62, 65], which causes the scaffold to release Ca^{2+} and

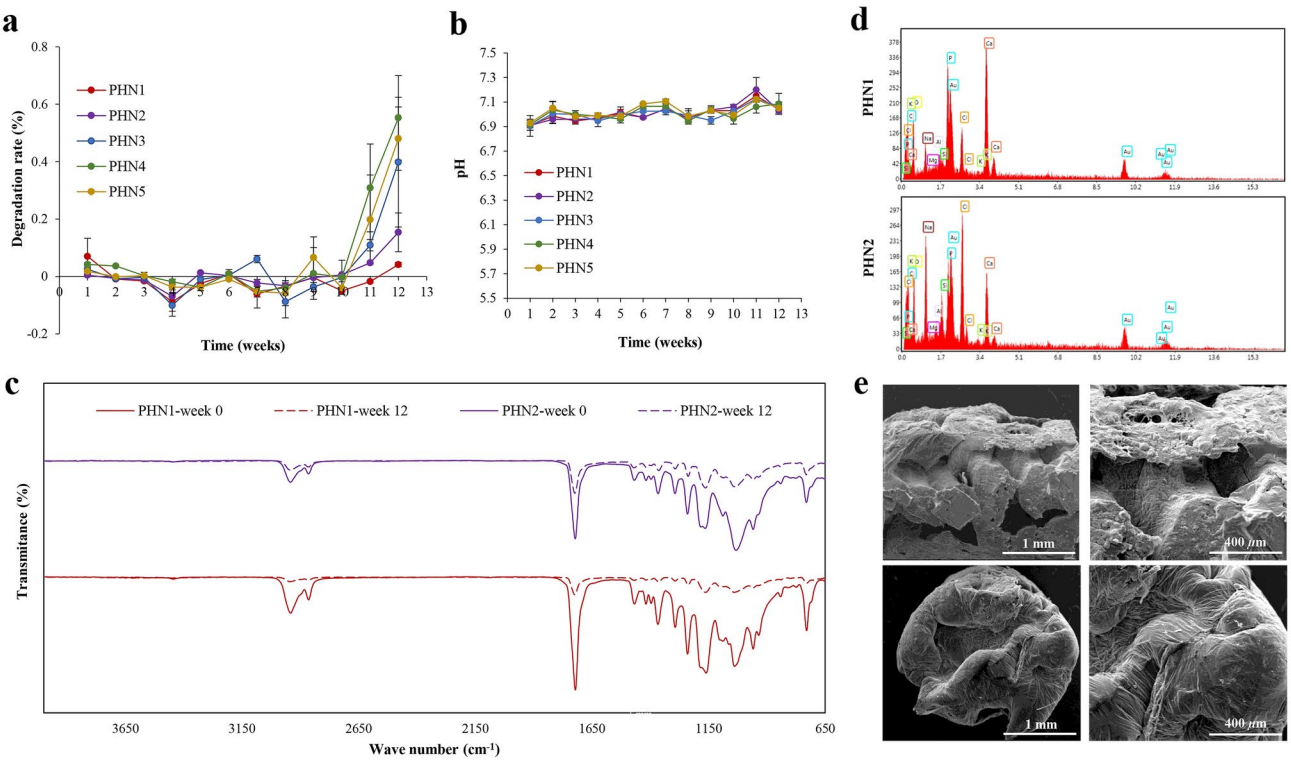

Fig. 5 **a** Degradation rate and **b** the pH changes after soaking the PHN1 to PHN5 nanocomposite scaffolds in PBS during 3 months. **c** FTIR spectra of the degraded PHN1 and PHN2 samples at 0 and 12 weeks following PBS immersion. **d** EDX analysis and **e** SEM images of PHN1 and PHN2 samples after 3 months of degradation in PBS at various scale bars. (Values are mean±*SD*, $n=3$, $^*P \leq 0.05$)

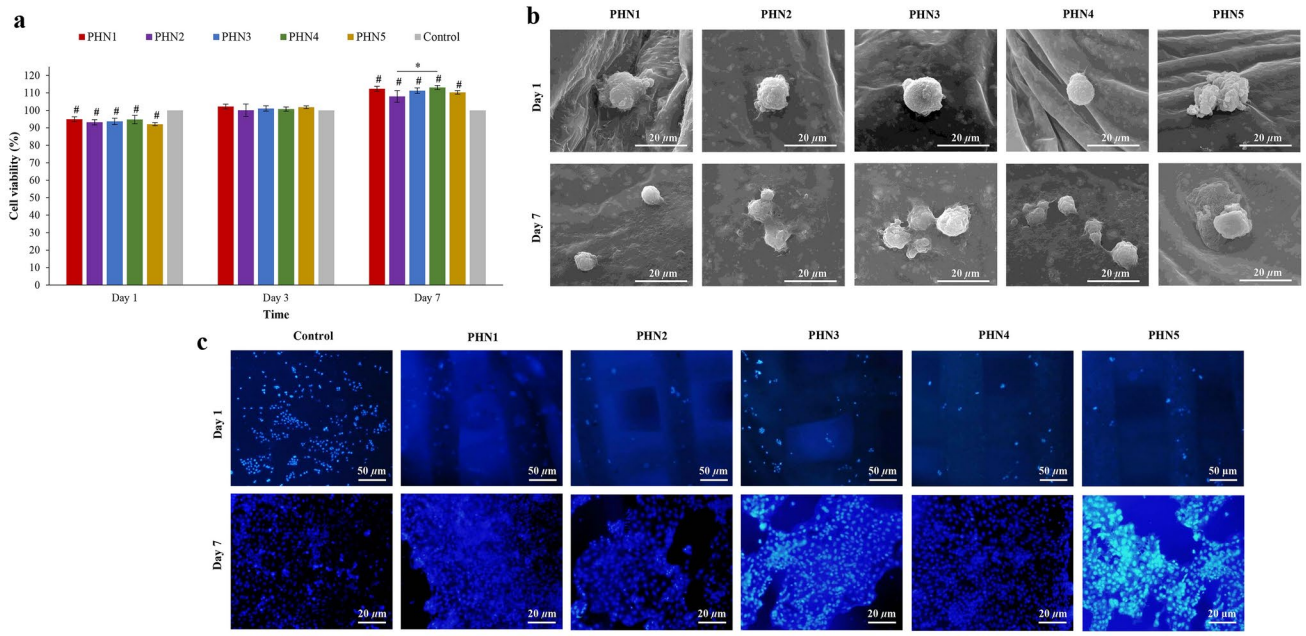

Fig. 6 **a** Viability analysis of MG-63 cells seeded on the 3D-printed nanocomposite scaffolds after 1, 3, and 7 days (values are presented as mean ± SD, $n = 3$, $^{*}P \leq 0.05$). The number sign ($^{\#}P \leq 0.05$) indicates a statistically significant difference compared to the control group. **b** SEM images of the scaffolds seeded with MG-63 cells. **c** DAPI-stained MG-63 cells on PHN1 to PHN5 samples after 1 and 7 days, shown at different scale bars

HPO_4^{2-} into the solution. Throughout the degradation process, pH levels remained within the physiological range, and the solution subsequently regained its buffered state.

In the FTIR spectrum (Fig. 5c) of PHN1 and PHN2 samples after 12 weeks, the intensities of the PCL peaks at 2865, 2941, and 1721 cm^{-1}, which correspond to CH_2 and C=O stretching vibrations, were reduced. This decrease in peak height indicates that the incorporation of NC and NHA nanoparticles in the scaffolds has resulted in an increase in the degradation of PCL. The heightened peaks of 1727 and 795 cm^{-1}, induced by the existence of NHA and NC, have also exhibited a decline in all scaffolds. This decrease may be attributed to the gradual release of these nanoparticles from the scaffolds. The observed changes in FTIR spectra suggest some degradation and ion release, although the structural integrity of the scaffold remained largely intact, as evidenced by the minor weight loss over the 12-week period. In general, no other obvious differences were observed, suggesting that the samples did not encounter any structural or chemical alterations.

The results of the EDX of the degraded samples (Fig. 5d) subsequent to a 3-month period further revealed a reduction in the quantity of calcium, phosphorus, and silicide ions present on the scaffolds' surface. This suggests the degradation of the scaffolds and the dissolution of anions and cations from the sample's surface into the solution. The PHN1 sample exhibited a diminished reduction in the levels of calcium and phosphorus elements, aligning with the observations derived from the degradation rate analysis of this particular sample, signifying a delayed degradation process.

SEM images (Fig. 5e) of all samples conspicuously illustrated the degraded surfaces subsequent to a 12-week period of immersion in PBS. The scaffolds exhibited evident signs of degradation, with their surfaces displaying observable holes and cracks, thereby revealing a rough matrix attributed to hydrolytic degradation. Prior studies have indicated that NHA incorporation enhances water and solvent flow across the NHA-PCL interface, increasing water infiltration into the PCL matrix and accelerating degradation [53]. Moreover, the existence of NC also promotes the absorption of water, thereby preparing PCL chains for hydrolysis and accelerating the degradation of PCL scaffolds [56].

3.8 Cellular Viability and Attachment on the Nanocomposite Scaffolds

Cell viability of each 3D-printed sample was assessed at 1, 3, and 7 days using the MTT assay (Fig. 6a). After 3 days, all scaffolds exhibited a cell viability rate that exceeded 100%, suggesting high biocompatibility of the scaffolds [66]. On days 1 and 3, it was observed that the PHN1 sample, exhibited the highest level of cell viability. However, all scaffolds demonstrated a statistically significant increase in cell viability rate over the control group after one week ($P \leq 0.05$), and the PHN4 sample exhibited the highest

percentage of MG-63 cell viability (113.05 ± 1.18%). The findings of the study also demonstrated that the NHA/NC 70:30 scaffold exhibited considerably superior cell viability, when compared to the NHA/NC 30:70 scaffold ($P \leq 0.05$). The lower cell viability in PCL/NC may be due to MMT toxicity at high concentrations, as shown in previous studies, whereas lower MMT concentrations did not reduce cell viability [67]. In general, the application of NC has been shown to enhance scaffold biocompatibility, promoting cellular proliferation and differentiation [68]. Moreover, it is noteworthy to mention that NHA has been identified as a highly efficacious nanoparticle in promoting cell proliferation, owing to its ability to enhance the concentration of indigenous Ca^{2+} and thereby trigger the proliferation of osteoblasts [2, 9, 69]. These results align with cell staining observations, which showed a significant increase in cell populations within each scaffold after one week, compared to the control group. Overall, the combination of NHA with an optimal amount of NC generates a structure conducive to enhanced cellular proliferation.

To evaluate in vitro biological performance, MG-63 cells were cultured and seeded onto each scaffold. The morphological characteristics of the cells after 1 and 7 days of culture are depicted in Fig. 6b. The findings of the investigation revealed that the cultured cells displayed excellent adherence to all of the scaffolds and evinced an extended cellular morphology and architecture that expanded towards the scaffolds through the formation of pseudopodia. Notably, scaffolds incorporating both NHA and NC showed enhanced cellular attachment, with pronounced lamellipodia and filopodia extensions by day 7, indicating robust cellular adhesion and proliferation.

DAPI, a fluorescent DNA probe, was employed to label the nuclei of viable MG-63 cells cultured on 3D-printed scaffolds for 1 and 7 days (Fig. 6c). After a week-long incubation, a substantial population of cells, characterized by a homogeneous morphology, were observed to have efficiently adhered and expanded onto the surface of the scaffolds. The findings of the study revealed a noteworthy increase in cellular proliferation on each scaffold in comparison to the control group after 7 days. Previous investigations have established that both NHA and NC exert a positive effect on cell adhesion and proliferation. Similar to NHA, the modified MMT has the ability to provide many active sites for the adsorption of adhesion molecules, such as vitronectin or fibronectin, and accelerate the diffusion of actin filaments of bone cells on the scaffolds [59, 70]. Furthermore, they can augment the surface area and roughness, which enhances cell adherence to the scaffolds [11, 69]. The elevated concentration of Ca^{2+} or Mg^{2+} along the surfaces of NC may potentially lead to improved cell adhesion. This is due to the role of these cations in facilitating interactions between cells and the through integrins [59, 71].

4 Conclusion

In the current study, PCL composite scaffolds with different NHA and NC concentrations were fabricated using 3D printing technology. Subsequently, the physicochemical and cellular properties of these scaffolds were evaluated in vitro. The SEM micrographs of the synthesized scaffolds exhibited interconnected rectangular macropores with the most and least porosity percentages for the PHN4 and PHN3 samples, respectively, which can be attributed to the ink's viscosity. As the concentration of NC was elevated, the hydrophilicity of the scaffolds was significantly enhanced. Furthermore, the inclusion of NC in the nanocomposite scaffolds led to an enhancement in water uptake, mechanical properties (reaching the level of spongy bone strength), and biodegradability. Since the scaffold compounds exhibited favorable bioactivity, the in vitro cultivation of MG-63 cells also demonstrated improved adhesion, proliferation, and viability within scaffolds comprised of NHA and NC after a period of 7 days. These findings indicated that the 3D-printed scaffolds, particularly when enriched with higher concentrations of NC, hold promising potential for the regeneration of bone defects.

Author Contributions Saba Nazari: Conceptualization, methodology, validation, formal analysis, writing Original draft. Dr.Seyed Ali Poursamar: methodology, validation, formal analysis. Dr. Mohammed Rafenia and Dr.Mitra Naeimi: Conceptualization, methodology, validation, writing review, and editing. Dr. Majid Monajjemi: Writing review and editing.

Funding This research did not receive any specific grant from funding agencies in the public, commercial, or not-for-profit sectors.

Data Availability The authors declare that all data supporting the findings of this study are available within the article.

Declarations

Competing Interests The authors have no competing interests to declare that are relevant to the content of this article.

References

1. Bigham, A., Aghajanian, A. H., Saudi, A., & Rafienia, M. (2020). Hierarchical porous Mg_2SiO_4–$CoFe_2O_4$ nanomagnetic scaffold for bone cancer therapy and regeneration: Surface modification and in vitro studies. *Materials Science and Engineering: C,109*, 110579. https://doi.org/10.1016/j.msec.2019.110579
2. Sattary, M., Kefayat, A., Bigham, A., & Rafienia, M. (2022). Polycaprolactone/gelatin/hydroxyapatite nanocomposite scaffold

seeded with stem cells from human exfoliated deciduous teeth to enhance bone repair: In vitro and in vivo studies. *Materials Technology,37*(5), 302–315. https://doi.org/10.1080/10667857.2020.1837488

3. Babaei, M., Jamshidi, N., Amiri, F., & Rafienia, M. (2022). Effects of low-intensity pulsed ultrasound stimulation on cell seeded 3D hybrid scaffold as a novel strategy for meniscus regeneration: An in vitro study. *Journal of Tissue Engineering and Regenerative Medicine,16*(9), 812–824. https://doi.org/10.1002/term.3331
4. Ghassemi, T., Shahroodi, A., Ebrahimzadeh, M. H., Mousavian, A., Movaffagh, J., & Moradi, A. (2018). Current concepts in scaffolding for bone tissue engineering. *Archives of Bone and Joint Surgery,6*(2), 90. https://doi.org/10.22038/abjs.2018.26340.1713
5. Cakmak, A. M., Unal, S., Sahin, A., Oktar, F. N., Sengor, M., Ekren, N., Gunduz, O., & Kalaskar, D. M. (2020). 3D printed polycaprolactone/gelatin/bacterial cellulose/hydroxyapatite composite scaffold for bone tissue engineering. *Polymers,12*(9), 1962. https://doi.org/10.3390/polym12091962
6. Li, P., Ruan, L., Wang, R., Liu, T., Song, G., Gao, X., Jiang, G., & Liu, X. (2021). Electrospun scaffold of collagen and polycaprolactone containing ZnO quantum dots for skin wound regeneration. *Journal of Bionic Engineering,18*, 1378–1390. https://doi.org/10.1007/s42235-021-00115-7
7. Mehdikhani, M., Yilgör, P., Poursamar, S. A., Etemadi, N., Gokyer, S., Navid, S., Farzan, M., Farzan, M., Babaei, M., & Rafienia, M. (2024). A hybrid 3D-printed and electrospun bilayer pharmaceutical membrane based on polycaprolactone/chitosan/polyvinyl alcohol for wound healing applications. *International Journal of Biological Macromolecules,282*, 136692. https://doi.org/10.1016/j.ijbiomac.2024.136692
8. Kazemi, M., Mirzadeh, M., Esmaeili, H., Kazemi, E., Rafienia, M., & Poursamar, S. A. (2024). Evaluation of the morphological effects of hydroxyapatite nanoparticles on the rheological properties and printability of hydroxyapatite/polycaprolactone nanocomposite inks and final scaffold features. *3D Printing and Additive Manufacturing,11*(1), 132–142. https://doi.org/10.1089/3dp.2021.0292
9. Shi, H., Zhou, Z., Li, W., Fan, Y., Li, Z., & Wei, J. (2021). Hydroxyapatite based materials for bone tissue engineering: A brief and comprehensive introduction. *Crystals,11*(2), 149. https://doi.org/10.3390/cryst11020149
10. Babaei, M., Ebrahim-Najafabadi, N., Mirzadeh, M., Abdali, H., Farnaghi, M., Gharavi, M. K., Kheradmandfard, M., Kharazi, A. Z., & Poursamar, S. A. (2024). A comprehensive bench-to-bed look into the application of gamma-sterilized 3D-printed polycaprolactone/hydroxyapatite implants for craniomaxillofacial defects, an in vitro, in vivo, and clinical study. *Biomaterials Advances,161*, 213900. https://doi.org/10.1016/j.bioadv.2024.213900
11. Wu, M., Chen, F., Wu, P., Yang, Z., Zhang, S., Xiao, L., Deng, Z., Zhang, C., Chen, Y., & Cai, L. (2021). Nanoclay mineral-reinforced macroporous nanocomposite scaffolds for in situ bone regeneration: In vitro and in vivo studies. *Materials & Design,205*, 109734. https://doi.org/10.1016/j.matdes.2021.109734
12. Amiri, F., Babaei, M., Jamshidi, N., Agheb, M., Rafienia, M., & Kazemi, M. (2022). Fabrication and assessment of a novel hybrid scaffold consisted of polyurethane-gellan gum-hyaluronic acid-glucosamine for meniscus tissue engineering. *International Journal of Biological Macromolecules,203*, 610–622. https://doi.org/10.1016/j.ijbiomac.2022.01.091
13. Wang, C., Huang, W., Zhou, Y., He, L., He, Z., Chen, Z., He, X., Tian, S., Liao, J., & Lu, B. (2020). 3D printing of bone tissue engineering scaffolds. *Bioactive Materials,5*(1), 82–91. https://doi.org/10.1016/j.bioactmat.2020.01.004
14. Zhang, B., Pei, X., Song, P., Sun, H., Li, H., Fan, Y., Jiang, Q., Zhou, C., & Zhang, X. (2018). Porous bioceramics produced by inkjet 3D printing: Effect of printing ink formulation on the ceramic macro and micro porous architectures control. *Composites Part B: Engineering,155*, 112–121. https://doi.org/10.1016/j.compositesb.2018.08.047
15. Sultana, T., Rana, M., Akhtar, M., Hasan, Z., Talukder, A., & Aseduzzaman, S. (2017). Preparation and physicochemical characterization of nano-hydroxyapatite based 3D porous scaffold for biomedical application. *Advances in Tissue Engineering and Regenerative Medicine,3*(3), 384–389. https://doi.org/10.15406/atroa.2017.03.00065
16. Ganesh, M., Aziz, A. S., Ubaidulla, U., Hemalatha, P., Saravanakumar, A., Ravikumar, R., Peng, M. M., Choi, E. Y., & Jang, H. T. (2016). Sulfanilamide and silver nanoparticles-loaded polyvinyl alcohol-chitosan composite electrospun nanofibers: Synthesis and evaluation on synergism in wound healing. *Journal of Industrial and Engineering Chemistry,39*, 127–135. https://doi.org/10.1016/j.jiec.2016.05.021
17. Kokubo, T., & Takadama, H. (2006). How useful is SBF in predicting in vivo bone bioactivity? *Biomaterials,27*(15), 2907–2915. https://doi.org/10.1016/j.biomaterials.2006.01.017
18. Zhou, X., Pan, Y., Liu, R., Luo, X., Zeng, X., Zhi, D., Li, J., Cheng, Q., Huang, Z., & Zhang, H. (2019). Biocompatibility and biodegradation properties of polycaprolactone/polydioxanone composite scaffolds prepared by blend or co-electrospinning. *Journal of Bioactive and Compatible Polymers,34*(2), 115–130. https://doi.org/10.1177/0883911519835569
19. Wandiyanto, J. V., Truong, V. K., Al Kobaisi, M., Juodkazis, S., Thissen, H., Bazaka, O., Bazaka, K., Crawford, R. J., & Ivanova, E. P. (2019). The fate of osteoblast-like MG-63 cells on pre-infected bactericidal nanostructured titanium surfaces. *Materials,12*(10), 1575. https://doi.org/10.3390/ma12101575
20. Chen, G., & Kawazoe, N. (2016). Preparation of polymer scaffolds by ice particulate method for tissue engineering. *Biomaterials nanoarchitectonics* (pp. 77–95). William Andrew Publishing.
21. Sun, J., Vijayavenkataraman, S., & Liu, H. (2017). An overview of scaffold design and fabrication technology for engineered knee meniscus. *Materials,10*(1), 29. https://doi.org/10.3390/ma10010029
22. Alexa, R. L., Iovu, H., Trica, B., Zaharia, C., Serafim, A., Alexandrescu, E., Radu, I.-C., Vlasceanu, G., Preda, S., & Ninciuleanu, C. M. (2021). Assessment of naturally sourced mineral clays for the 3D printing of biopolymer-based nanocomposite inks. *Nanomaterials,11*(3), 703. https://doi.org/10.3390/nano11030703
23. Sandri, G., Faccendini, A., Longo, M., Ruggeri, M., Rossi, S., Bonferoni, M. C., Miele, D., Prina-Mello, A., Aguzzi, C., & Viseras, C. (2020). Halloysite-and montmorillonite-loaded scaffolds as enhancers of chronic wound healing. *Pharmaceutics,12*(2), 179. https://doi.org/10.3390/pharmaceutics12020179
24. Friedrich, L. M., & Seppala, J. E. (2021). Simulated filament shapes in embedded 3D printing. *Soft Matter,17*(35), 8027–8046. https://doi.org/10.1039/D1SM00731A
25. Aydin, E. M., Kara, B., Bundur, Z. B., Ozyurt, N., Bebek, O., & Gulgun, M. A. (2022). A comparative evaluation of sepiolite and nano-montmorillonite on the rheology of cementitious materials for 3D printing. *Construction and Building Materials,350*, 128935. https://doi.org/10.1016/j.conbuildmat.2022.128935
26. Gao, Q., Niu, X., Shao, L., Zhou, L., Lin, Z., Sun, A., Fu, J., Chen, Z., Hu, J., & Liu, Y. (2019). 3D printing of complex GelMA-based scaffolds with nanoclay. *Biofabrication,11*(3), 035006. https://doi.org/10.1088/1758-5090/ab0cf6
27. Ianchis, R., Marin, M. M., Alexa, R. L., Gifu, I. C., Alexandrescu, E., Pircalabioru, G. G., Vlasceanu, G. M., Teodorescu, G. M., Serafim, A., & Preda, S. (2023). Nanoclay-reinforced alginate/salecan composite inks for 3D printing applications. *International*

Journal of Bioprinting,10(1), 0967. https://doi.org/10.36922/ijb.0967

28. Murphy, C. M., & O'Brien, F. J. (2010). Understanding the effect of mean pore size on cell activity in collagen-glycosaminoglycan scaffolds. *Cell Adhesion & Migration,4*(3), 377–381. https://doi.org/10.4161/cam.4.3.11747
29. Shanthi, P. M. S., Ashok, M., Balasubramanian, T., Riyasdeen, A., & Akbarsha, M. (2009). Synthesis and characterization of nano-hydroxyapatite at ambient temperature using cationic surfactant. *Materials Letters,63*(24–25), 2123–2125. https://doi.org/10.1016/j.matlet.2009.07.008
30. Yu, C., Ke, Y., Hu, X., Zhao, Y., Deng, Q., & Lu, S. (2019). Effect of bifunctional montmorillonite on the thermal and tribological properties of polystyrene/montmorillonite nanocomposites. *Polymers,11*(5), 834. https://doi.org/10.3390/polym11050834
31. Baghbadorani, M. A., Bigham, A., Rafienia, M., & Salehi, H. (2021). A ternary nanocomposite fibrous scaffold composed of poly (ε-caprolactone)/gelatin/gehlenite ($Ca_2Al_2SiO_7$): Physical, chemical, and biological properties in vitro. *Polymers for Advanced Technologies,32*(2), 582–598. https://doi.org/10.1002/pat.5113
32. Ji, Y., Liang, K., Shen, X., & Bowlin, G. L. (2014). Electrospinning and characterization of chitin nanofibril/polycaprolactone nanocomposite fiber mats. *Carbohydrate Polymers,101*, 68–74. https://doi.org/10.1016/j.carbpol.2013.09.012
33. Sattary, M., Khorasani, M. T., Rafienia, M., & Rozve, H. S. (2018). Incorporation of nanohydroxyapatite and vitamin D3 into electrospun PCL/gelatin scaffolds: The influence on the physical and chemical properties and cell behavior for bone tissue engineering. *Polymers for Advanced Technologies,29*(1), 451–462. https://doi.org/10.1002/pat.4134
34. Khodamoradi, N., Babaeipour, V., & Sirousazar, M. (2019). Bacterial cellulose/montmorillonite bionanocomposites prepared by immersion and in-situ methods: Structural, mechanical, thermal, swelling and dehydration properties. *Cellulose,26*(13), 7847–7861. https://doi.org/10.1007/s10570-019-02666-9
35. Li, D., Li, P., Xu, Y., Guo, W., Li, M., Chen, M., Wang, H., & Lin, H. (2022). Progress in montmorillonite functionalized artificial bone scaffolds: Intercalation and interlocking, nanoenhancement, and controlled drug release. *Journal of Nanomaterials,2022*(1), 7900382. https://doi.org/10.1155/2022/7900382
36. Yazdanpanah, Z., Johnston, J. D., Cooper, D. M., & Chen, X. (2022). 3D bioprinted scaffolds for bone tissue engineering: State-of-the-art and emerging technologies. *Frontiers in Bioengineering and Biotechnology,10*, 824156. https://doi.org/10.3389/fbioe.2022.824156
37. Bossard, C., Granel, H., Wittrant, Y., Jallot, É., Lao, J., Vial, C., & Tiainen, H. (2018). Polycaprolactone/bioactive glass hybrid scaffolds for bone regeneration. *Biomedical Glasses,4*(1), 108–122. https://doi.org/10.1515/bglass-2018-0010
38. Yazdanpanah, Z., Sharma, N. K., Raquin, A., Cooper, D. M., Chen, X., & Johnston, J. D. (2023). Printing tissue-engineered scaffolds made of polycaprolactone and nano-hydroxyapatite with mechanical properties appropriate for trabecular bone substitutes. *Biomedical Engineering Online,22*(1), 73. https://doi.org/10.1186/s12938-023-01135-6
39. Jahir-Hussain, M. J., Maaruf, N. A., Esa, N. E. F., & Jusoh, N. (2021). The effect of pore geometry on the mechanical properties of 3D-printed bone scaffold due to compressive loading. *IOP Conference Series: Materials Science and Engineering,1051*(1), 012016. https://doi.org/10.1088/1757-899X/1051/1/012016
40. Karimi, M., Asadi-Eydivand, M., Abolfathi, N., Chehrehsaz, Y., & Solati-Hashjin, M. (2023). The effect of pore size and layout on mechanical and biological properties of 3D-printed bone scaffolds with gradient porosity. *Polymer Composites,44*(2), 1343–1359. https://doi.org/10.1002/pc.27174
41. Abulyazied, D. E., & Ene, A. (2021). An investigative study on the progress of nanoclay-reinforced polymers: Preparation, properties, and applications: A review. *Polymers,13*(24), 4401. https://doi.org/10.3390/polym13244401
42. Rezapourian, M., Kamboj, N., Jasiuk, I., & Hussainova, I. (2022). Biomimetic design of implants for long bone critical-sized defects. *Journal of the Mechanical Behavior of Biomedical Materials*. https://doi.org/10.1016/j.jmbbm.2022.105370
43. Xu, W., Lu, X., Hayat, M. D., Tian, J., Huang, C., Chen, M., Qu, X., & Wen, C. (2019). Fabrication and properties of newly developed $Ti_{35}Zr_{28}Nb$ scaffolds fabricated by powder metallurgy for bone-tissue engineering. *Journal of Materials Research and Technology,8*(5), 3696–3704. https://doi.org/10.1016/j.jmrt.2019.06.021
44. Liao, C., Li, Y., & Tjong, S. C. (2020). Polyetheretherketone and its composites for bone replacement and regeneration. *Polymers,12*(12), 2858. https://doi.org/10.3390/polym12122858
45. Zimina, A., Senatov, F., Choudhary, R., Kolesnikov, E., Anisimova, N., Kiselevskiy, M., Orlova, P., Strukova, N., Generalova, M., & Manskikh, V. (2020). Biocompatibility and physico-chemical properties of highly porous PLA/HA scaffolds for bone reconstruction. *Polymers,12*(12), 2938. https://doi.org/10.3390/polym12122938
46. Guy, O. J., & Walker, K.-A.D. (2016). Silicon carbide biotechnology. *Chapter 4-graphene functionalization for biosensor applications* (pp. 85–141). Elsevier.
47. Karizmeh, M. S., Poursamar, S. A., Kefayat, A., Farahbakhsh, Z., & Rafienia, M. (2022). An in vitro and in vivo study of PCL/chitosan electrospun mat on polyurethane/propolis foam as a bilayer wound dressing. *Biomaterials Advances,135*, 112667. https://doi.org/10.1016/j.msec.2022.112667
48. Nitya, G., Nair, G. T., Mony, U., Chennazhi, K. P., & Nair, S. V. (2012). In vitro evaluation of electrospun PCL/nanoclay composite scaffold for bone tissue engineering. *Journal of Materials Science: Materials in Medicine,23*, 1749–1761. https://doi.org/10.1007/s10856-012-4647-x
49. Rajzer, I. (2014). Fabrication of bioactive polycaprolactone/hydroxyapatite scaffolds with final bilayer nano-/micro-fibrous structures for tissue engineering application. *Journal of Materials Science,49*, 5799–5807. https://doi.org/10.1007/s10853-014-8311-3
50. Xia, Y., Zhou, P., Cheng, X., Xie, Y., Liang, C., Li, C., & Xu, S. (2013). Selective laser sintering fabrication of nano-hydroxyapatite/poly-ε-caprolactone scaffolds for bone tissue engineering applications. *International Journal of Nanomedicine,8*, 4197–4213. https://doi.org/10.2147/IJN.S50685
51. An, J. H., & Kim, H. Y. (2024). Scaffolds bioink for 3D bioprinting. *Food Science of Animal Resources,45*(1), 126–144. https://doi.org/10.5851/kosfa.2024.e120
52. Dana, K., & Sarkar, M. (2020). Organophilic nature of nanoclay. *Clay nanoparticles* (pp. 117–138). Elsevier.
53. Trakoolwannachai, V., Kheolamai, P., & Ummartyotin, S. (2019). Characterization of hydroxyapatite from eggshell waste and polycaprolactone (PCL) composite for scaffold material. *Composites Part B: Engineering,173*, 106974. https://doi.org/10.1016/j.compositesb.2019.106974
54. Li, B., Ren, K., Wang, Y., Qi, Y., Chen, X., & Huang, Y. (2016). Protein-cross-linked hydrogels with tailored swelling and bioactivity performance: A comparative study. *ACS Applied Materials & Interfaces,8*(45), 30788–30796. https://doi.org/10.1021/acsami.6b11287
55. Zadehnajar, P., Akbari, B., Karbasi, S., & Mirmusavi, M. H. (2020). Preparation and characterization of poly ε-caprolactone-gelatin/multi-walled carbon nanotubes electrospun scaffolds for cartilage tissue engineering applications. *International Journal*

of Polymeric Materials and Polymeric Biomaterials,69(5), 326–337. https://doi.org/10.1080/00914037.2018.1563088
56. Gaharwar, A. K., Mukundan, S., Karaca, E., Dolatshahi-Pirouz, A., Patel, A., Rangarajan, K., Mihaila, S. M., Iviglia, G., Zhang, H., & Khademhosseini, A. (2014). Nanoclay-enriched poly (ε-caprolactone) electrospun scaffolds for osteogenic differentiation of human mesenchymal stem cells. *Tissue Engineering Part A,20*(15–16), 2088–2101. https://doi.org/10.1089/ten.tea.2013.028
57. Naga, S., Mahmoud, E., El-Maghraby, H., El-Kady, A. M., Arbid, M., Killinger, A., & Gadow, R. (2018). Porous scaffolds based on biogenic poly (ε-caprolactone)/hydroxyapatite composites: In vivo study. *Advances in Natural Sciences: Nanoscience and Nanotechnology,9*(4), 045004. https://doi.org/10.1088/2043-6254/aae9f7
58. Olad, A., & Azhar, F. F. (2014). The synergetic effect of bioactive ceramic and nanoclay on the properties of chitosan–gelatin/nanohydroxyapatite–montmorillonite scaffold for bone tissue engineering. *Ceramics International,40*(7), 10061–10072. https://doi.org/10.1016/j.ceramint.2014.04.010
59. Mousa, M., Evans, N. D., Oreffo, R. O., & Dawson, J. I. (2018). Clay nanoparticles for regenerative medicine and biomaterial design: A review of clay bioactivity. *Biomaterials,159*, 204–214. https://doi.org/10.1016/j.biomaterials.2017.12.024
60. Aktug, S. L., Durdu, S., Aktas, S., Yalcin, E., & Usta, M. (2019). Surface and in vitro properties of Ag-deposited antibacterial and bioactive coatings on AZ31 Mg alloy. *Surface and Coatings Technology,375*, 46–53. https://doi.org/10.1016/j.surfcoat.2019.07.013
61. Polo-Corrales, L., Latorre-Esteves, M., & Ramirez-Vick, J. E. (2014). Scaffold design for bone regeneration. *Journal of Nanoscience and Nanotechnology,14*(1), 15–56. https://doi.org/10.1166/jnn.2014.9127
62. Mirmusavi, M. H., Ahmadian, M., & Karbasi, S. (2022). Polycaprolactone-chitosan/multi-walled carbon nanotube: A highly strengthened electrospun nanocomposite scaffold for cartilage tissue engineering. *International Journal of Biological Macromolecules,209*, 1801–1814. https://doi.org/10.1016/j.ijbiomac.2022.04.152
63. Zhang, Q., Jiang, Y., Zhang, Y., Ye, Z., Tan, W., & Lang, M. (2013). Effect of porosity on long-term degradation of poly (ε-caprolactone) scaffolds and their cellular response. *Polymer Degradation and Stability,98*(1), 209–218. https://doi.org/10.1016/J.POLYMDEGRADSTAB.2012.10.008
64. Azari, P., Hosseini, S., Murphy, B. P., & Martinez-Chapa, S. O. (2018). Electrospun biopolyesters: Hydrophobic scaffolds with favorable biological response. *Journal of Public Health International,1*, 5–9. https://doi.org/10.14302/issn.2641-4538.jphi-18-1975
65. Fathi, M., Hanifi, A., & Mortazavi, V. (2008). Preparation and bioactivity evaluation of bone-like hydroxyapatite nanopowder. *Journal of Materials Processing Technology,202*(1–3), 536–542. https://doi.org/10.1016/j.jmatprotec.2007.10.004
66. Eskandarinia, A., Kefayat, A., Gharakhloo, M., Agheb, M., Khodabakhshi, D., Khorshidi, M., Sheikhmoradi, V., Rafienia, M., & Salehi, H. (2020). A propolis enriched polyurethane-hyaluronic acid nanofibrous wound dressing with remarkable antibacterial and wound healing activities. *International Journal of Biological Macromolecules,149*, 467–476. https://doi.org/10.1016/j.ijbiomac.2020.01.255
67. Bekaroğlu, G. M., & İşçi, S. (2022). Raw and purified clay minerals for drug delivery applications. *ACS Omega,7*(43), 38825–38831. https://doi.org/10.1021/acsomega.2c04510
68. Huang, Y., Dan, N., Dan, W., & Zhao, W. (2019). Reinforcement of polycaprolactone/chitosan with nanoclay and controlled release of curcumin for wound dressing. *ACS Omega,4*(27), 22292–22301. https://doi.org/10.1021/acsomega.9b02217
69. Jaiswal, A., Chhabra, H., Soni, V., & Bellare, J. (2013). Enhanced mechanical strength and biocompatibility of electrospun polycaprolactone-gelatin scaffold with surface deposited nano-hydroxyapatite. *Materials Science and Engineering: C,33*(4), 2376–2385. https://doi.org/10.1016/j.msec.2013.02.003
70. Sato, M., Aslani, A., Sambito, M. A., Kalkhoran, N. M., Slamovich, E. B., & Webster, T. J. (2008). Nanocrystalline hydroxyapatite/titania coatings on titanium improves osteoblast adhesion. *Journal of Biomedical Materials Research Part A,84*(1), 265–272. https://doi.org/10.1002/jbm.a.31469
71. Hynes, R. O. (2002). Integrins: Bidirectional, allosteric signaling machines. *Cell,110*(6), 673–687. https://doi.org/10.1016/S0092-8674(02)00971-6